Bulletin of the Seismological Society of America, Vol. XX, No. XX, pp. –, – 2018, doi: 10.1785/0120180005

Ⓔ

# Validation of Deterministic Broadband Ground Motion and Variability from Dynamic Rupture Simulations of Buried Thrust Earthquakes

by Kyle B. Withers,*,† Kim B. Olsen, Zheqiang Shi, and Steven M. Day

Abstract We numerically model broadband ground motion (up to 5–7.5 Hz) from blind-thrust scenario earthquakes matching the fault geometry of the 1994 $M_w$ 6.7 Northridge earthquake. Several realizations are modeled (by varying the hypocenter location in the dynamic rupture simulation) in a 1D-layered velocity profile. In addition, we include $Q(f)$, nonlinear effects from Drucker–Prager plasticity, and superimpose small-scale medium complexity in both a 1D-layered and 3D velocity model within the subsequent wave propagation. We investigate characteristics of the ground motion and its variability up to 50 km from the fault by comparing them with ground-motion prediction equations (GMPEs), simple proxy metrics, as well as strong ground motion records from the Northridge event. We find that median ground motion closely follows the trend predicted by GMPEs and that the intraevent standard deviation, although varying with hypocenter location, lies near that of GMPE models. Plasticity affects ground-motion amplitudes in regions near the source, reducing intraevent variability above ~0.5 Hz. Heterogeneity in the velocity structure on both the regional and small scales is needed for the simulated data to match two proxy metrics: the period-to-period correlation of spectral acceleration (SA) and the ratio of maximum-to-median SA. Although small-scale heterogeneity has a negligible effect on median SA for this style of rupture, it serves to significantly increase the cumulative absolute velocity, better agreeing with observations. When compared with strong-motion data, we find that long-wavelength velocity structure within our deterministic simulations reduces bias at both short and long periods. Finally, synthetic ground motion at both footwall and hanging-wall sites has no clear dependence on the distance to rupture (at both short and long periods); directivity is likely overpowering any hanging-wall effect.

*Electronic Supplement:* Verification of the two-step procedure (converting slip-rate output from the dynamic rupture simulation to a kinematic source) for a dipping-thrust fault by comparing Support Operator Rupture Dynamics (SORD) and anelastic wave-propagation (AWP) time series and spectra, figures of cumulative absolute velocity (CAV) with intraevent variability, and spectral acceleration versus $R_x$ for averaged profiles within the fault strike.

## Introduction

Ground-motion time series are needed as input for nonlinear structural dynamic analysis of buildings and performance-based earthquake engineering. Realistic ground-motion synthetics may help verify or even improve ground-motion prediction equations (GMPEs) and reliably extend them into the distance range where only a few recordings exist, such as in the near field of large earthquakes. Earthquake simulations have become quite accurate at modeling ground motion at low frequencies (LFs) up to 1 Hz or so (e.g., Olsen, 2000; Roten *et al.*, 2011). Because of the prohibitive cost of fully deterministic broadband simulations, in recent years hybrid methodologies have been incorporated, combining a deterministic approach at LFs ($f < \sim 1$ Hz) with a stochastic approach at high frequencies (HFs; $f > \sim 1$ Hz). There are several techniques in use today, for example, Hartzell *et al.* (2005, 2010), Frankel (2009), Mai *et al.* (2010), Atkinson and Assatourians (2012), Anderson (2015), Crempien and Archuleta (2015),

*Now at U.S. Geological Survey, Geologic Hazards Science Center, 1711 Illinois Street, Golden, Colorado 80401.

†Also at Institute of Geophysics and Planetary Physics, 9500 Gilman Drive, University of California, San Diego, La Jolla, California 92093.

Graves and Pitarka (2015), and Olsen and Takedatsu (2015). One drawback of hybrid techniques is that the purely stochastic methods (at least for the HF) involve little physics in terms of parameterizing the earthquake rupture and details of wave propagation. With recent computational advances, it is now possible to deterministically model ground motion at significant distances from the source at higher frequencies (> 1 Hz). Modeling earthquake ground-motion prediction in this bandwidth helps determine seismic hazard for short buildings (< 10 stories) and other structures with high-resonant frequencies.

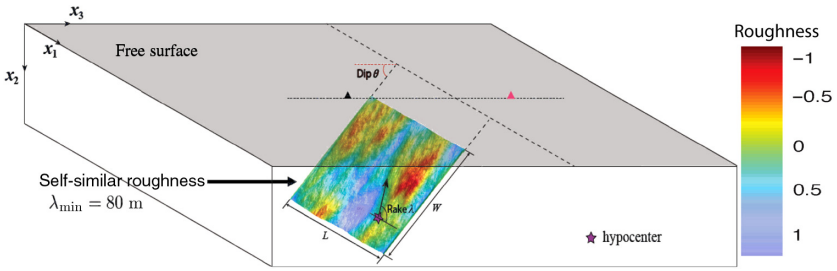


**Figure 1.** Rough-fault geometry of the dip-slip fault used in this study with geometry modeled off the dimensions of the 1994 Northridge earthquake. The rupture plane dips toward the southwest. The color version of this figure is available only in the electronic edition.

Previous authors studied the effect rough faults and 3D media complexity have on the rupture dynamics and ground motion. example, Hartzell *et al.* (2010) investigated the impact of small-scale heterogeneities superimposed on a background 3D velocity model for a finite-fault rupture of the Hayward fault, pointing out the limitations of predicting the range of ground motion at HFs. Shi and Day (2013) performed 3D dynamic rupture simulations along a rough fault and found that the synthetic broadband ground motion was comparable to that of empirical observations. More recently, Graves and Pitarka (2016) combined a rough-fault geometry with small-scale velocity perturbations in the medium (in a kinematic approach) and found that both of these complexities reduce coherency of ground motions above 1 Hz, leading to better agreement with observed data.

In the companion paper to this article, we previously modeled deterministic broadband ground motion in simulations incorporating rough-fault topography along a generic strike-slip fault (Withers *et al.*, 2018). That study found that small-scale fault geometry and media complexity, combined with frequency-dependent anelastic attenuation, can have a significant impact on amplitude and variability of ground-motion metrics, particularly at higher frequencies. In this work, we expand off the work we performed along a strike-slip fault using a similar approach, and study a blind-thrust fault with dimensions of the 1994 $M_w$ 6.7 Northridge earthquake. We model several realizations with similar moment magnitudes by varying the hypocenter location. Moment-rate time series derived from dynamic rupture models, simulated using the Support Operator Rupture Dynamics (SORD), are used as a kinematic source, inserted into the finite-difference anelastic wave-propagation code (AWP-ODC) with $Q(f)$. These simulations are performed in both a 1D-layered model characteristic of a southern California rock site and a 3D medium extracted from the Southern California Earthquake Center (SCEC) Community Velocity Model (CVM) including a surface geotechnical layer (GTL). Small-scale heterogeneity is included by superimposing a stochastic distribution onto the background velocity models. In addition to the source and medium components mentioned above, we incorporate nonlinear effects within the wave propagation via Drucker–Prager plasticity. We analyze the ground motion and intraevent variability influenced by scattering and nonlinear effects up to $R_{rup} = 50$ km from the fault. We validate our simulations with empirical observations such as Next Generation Attenuation (NGA) relations (GMPEs) and simple proxy metrics, as well as strong-motion data from the Northridge earthquake. The simulations in this study are not meant to describe the range of all possible ground motion by trying every permutation of parameters but rather to highlight the behavior that can become significant at frequencies > 1 Hz.

## Methods

Here, we discuss the specifics of the dynamic rupture and kinematic simulations, and highlights the initial conditions used for rupture and the components included during wave propagation.

### Dynamic Rupture Simulations

We perform 3D dynamic rupture simulations along rough faults to model the source process of the 1994 $M_w$ 6.7 Northridge earthquake using the the SORD code (Shi and Day, 2013). This event occurred along a blind-thrust fault in the San Fernando valley, about 20 miles northwest of downtown Los Angeles, with a maximum slip near 3 m. The epicenter was at a depth of 19 km, at the southeastern corner of a dipping fault plane, with rupture extending for a duration of ~10 s. The model setup and fault geometry are shown in Figure 1. Following Wald *et al.* (1996), the mean fault plane has a dip angle of 40° and strike of 122°. The surface topography of the dipping fault is assumed to follow a self-similar roughness pattern with wavelengths of 80 m up to the length of the fault and an amplitude-to-wavelength ratio of 0.02 (in the range observed for thrust faults, Candela *et al.*, 2012). A grid spacing of 20 m along the fault is used for the model discretization to resolve fault roughness and the cohesive zone of dynamic rupture, resulting in ~1.7 million subfaults. The fault slip is governed by a linear slip-weakening friction law with static friction coefficient $\mu_s = 0.4$, dynamic friction coefficient $\mu_d = 0.3$, and slip-weakening distance $D_c = 0.08$ m along the effective slip area of the fault. These values of parameters

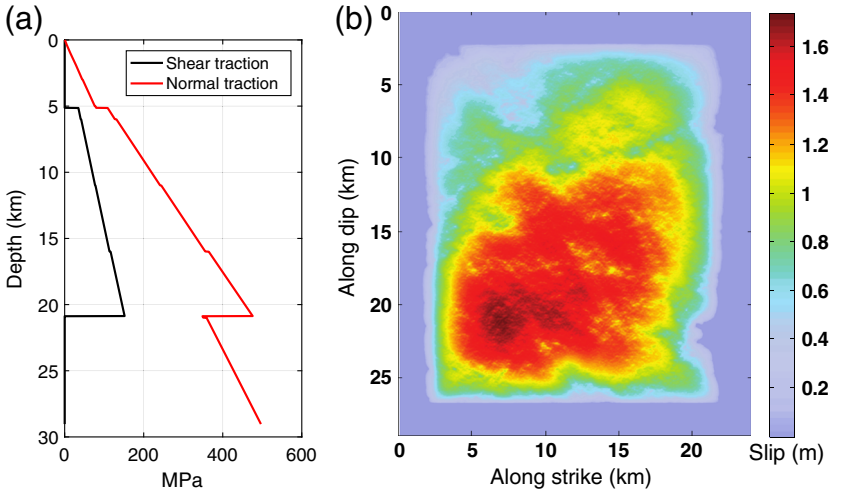


**Figure 2.** (a) Magnitudes of initial normal and shear tractions resolved onto the mean fault plane. (b) Average final slip along the fault (m) from the three events (there is negligible variation in the cumulative slip among the three hypocenter locations, because each rupture used the same initial stress conditions). The color version of this figure is available only in the electronic edition.

are within the typical ranges used in dynamic rupture simulations (albeit a somewhat smaller $D_c$ value was used here compared to many previous studies) and were found to be able to produce a final slip distribution with a moment magnitude close to that of the 1994 $M_w$ 6.7 Northridge event.

The dynamic friction coefficient is gradually increased to the level of the static coefficient along all sides of the fault surface to effectively constrain slip to dimensions representative of the Northridge rupture (20 km along-strike and 24.9 km along-dip, see Fig. 1) and depth to the top of the rupture 5 km below the free surface. A lithostatic background stress is assumed to produce slightly oblique reverse faulting with a rake angle of 105° (see Fig. 2a). Plasticity is only included within the subsequent wave propagation. The rupture is nucleated by imposing a circular shear traction perturbation with a radius of 1 km around the hypocenter. The same procedure is used in SCEC Rupture Dynamics Code Validation exercises that adopt rate-and-state friction (Harris *et al.*, 2009). The chosen amplitude and size of the nucleation patch is slightly above the threshold required to trigger a spontaneous rupture strong enough to propagate over the entire fault area.

We simulate three dynamic rupture scenarios using a characteristic hard-rock site profile with minimum $V_S = 863$ m/s (see Withers *et al.*, 2018; Fig. 1) to generate a few realizations of earthquakes for this fault geometry and stress conditions. The hypocenter locations are selected from plausible nucleation points, at depths near the base of the fault. Figure 2b plots the final slip for the rupture models (the amplitude and spatial pattern is almost identical for each hypocenter location because we used identical initial stress conditions). Figure 3 depicts the three hypocenter locations and corresponding peak slip rates. and Figure 4 plots the time histories of seismic moment rate for these elastic simulations. We will refer to these throughout the article as events 1–3. The evolution of slip rate along the rough fault from one of the simulations (event 1, matching that of the Northridge hypocenter location) is shown in Figure 5. Similar to the strike-slip rough-fault simulations performed in Shi and Day (2013), fault roughness-induced irregular rupture propagation generates HF radiation throughout the medium (Ⓔ Figs. S1 and S2, available in the electronic supplement to this article). Fourier spectra of the acceleration records (e.g., Ⓔ Fig. S2) indicate that the acceleration spectra are roughly flat between a few tenths of a Hz and an upper cutoff frequency of slightly less than 10 Hz. (We are able to resolve the HFs with SORD in Ⓔ Figs. S1 and S2 because the simulations were run in a homogenous medium, with $V_P = 6000$ m/s, $V_S = 3464$ m/s, and $\rho = 2.7$ kg/m$^3$. After verifying that the source has sufficient broadband energy, we then use the

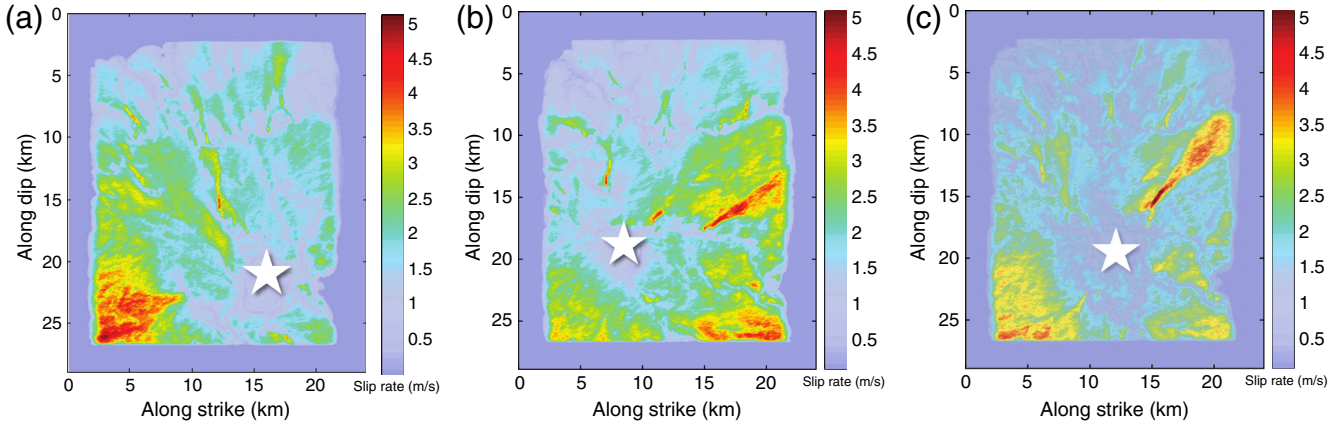


**Figure 3.** Maximum slip rate (m/s) for the three dynamic rupture models. (a) Event 1 (b) event 2, and (c) event 3. The star depicts the epicentral locations. The color version of this figure is available only in the electronic edition.

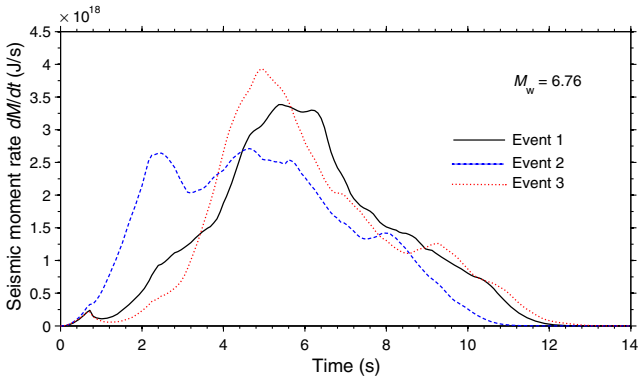


**Figure 4.** Moment rate time histories of the rupture scenarios with nucleation locations of events 1–3. Each event has the same magnitude. The color version of this figure is available only in the electronic edition.

above-mentioned 1D-layered rock site profile that includes lower velocities in the near surface, as the medium for the remaining dynamic ruptures in this article.)

## Kinematic Simulations

The slip-rate time series from the dynamic simulations performed in SORD are converted to double-couple point sources to generate broadband moment-rate time series for input into our wave-propagation code, AWP-ODC-GPU. This procedure allows for ground motion to be computed at farther distances from the fault because of the code's greater computationally efficiency. Additionally, we can include complexities within the media that currently SORD does not support (such as frequency-dependent anelastic attenuation). More details about this approach are discussed in the companion paper to this article, Withers *et al.* (2018). Ⓔ Figure S3 plots a comparison of the wave propagation between SORD and AWP, verifying that this technique remains accurate for a dipping fault and 1D-layered velocity structure (as an extension of the strike-slip fault in Withers *et al.*, 2018). Figure 6 plots the model domain chosen for this study, including nearby strong ground motion stations (as used in the SCEC Broadband Simulation Platform study, Goulet *et al.*, 2015) located within and near the study area. We simulate 100–140 s (depending on the velocity model) of ground motion and store time series on a grid at the free surface at a resolution of 80 m.

We ran the kinematic simulations in both 1D-layered (as used in the dynamic simulations) and 3D CVM background velocity models with and without small-scale medium heterogeneity (colored Gaussian noise with a von Karman autocorrelation), with varying statistical parameters, based on the approach outlined in Withers *et al.* (2018). Ⓔ Figure S4 plots an example of the media heterogeneity at the surface using the

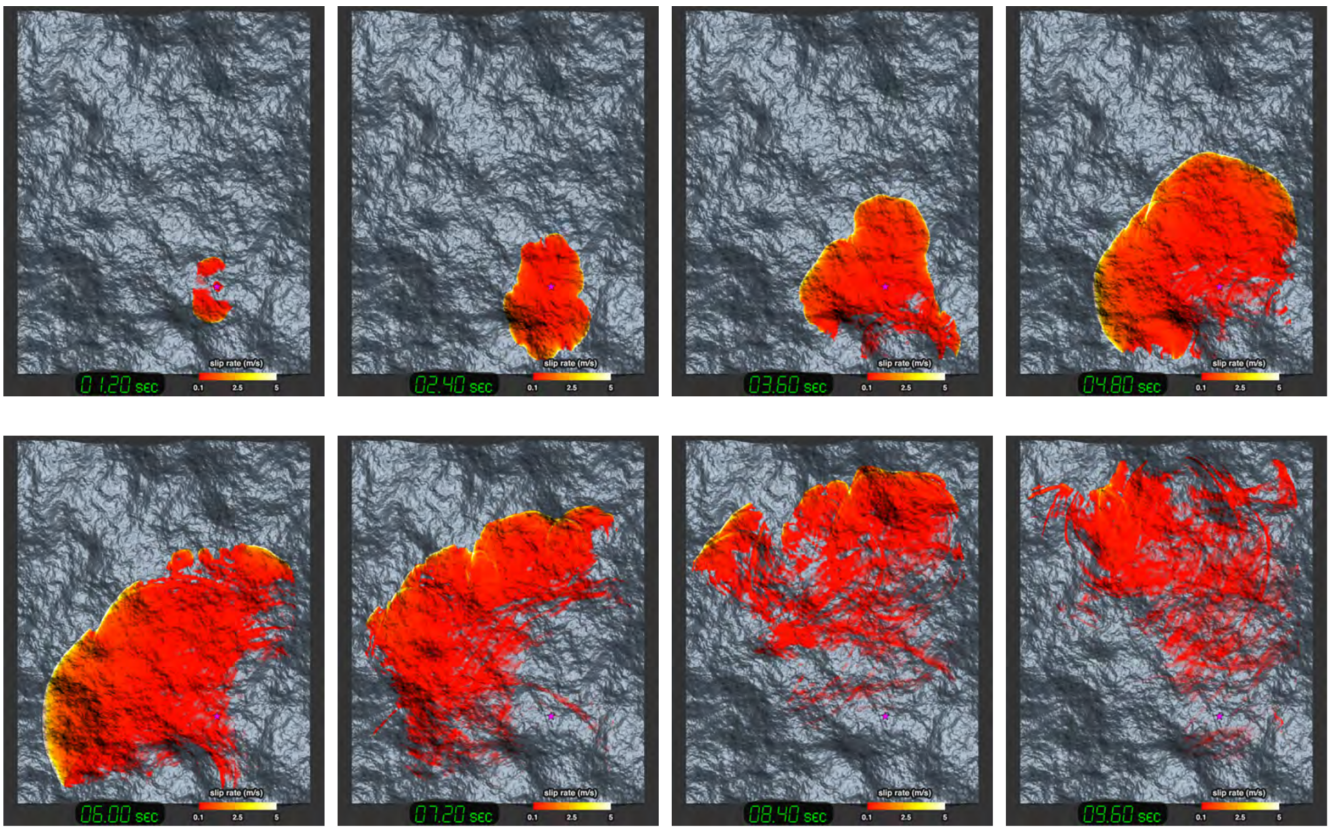


**Figure 5.** Snapshots of slip rates along the dipping rough fault every 1.2 s. The view angle is from the hanging wall toward the footwall. The color version of this figure is available only in the electronic edition.

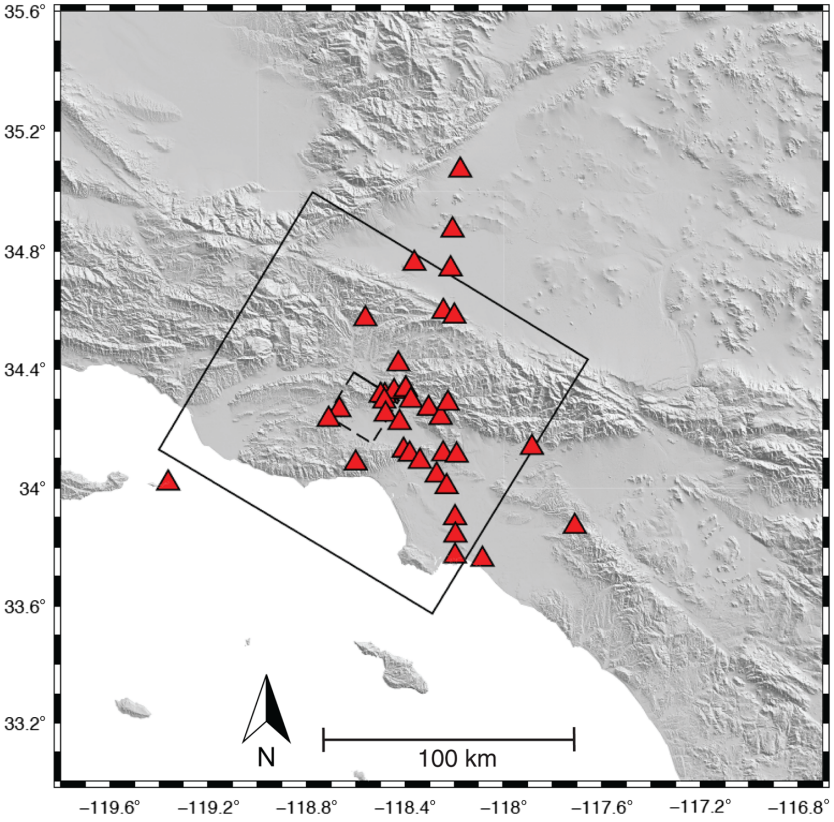


**Figure 6.** Simulation region location (large rectangle) with strong ground motion stations used in the Southern California Earthquake Center Broadband Simulation Platform (Goulet *et al.*, 2015) indicated by triangles; only stations within the simulation domain are used within this study. The smaller dashed box indicates the vertical projection of the rupture plane to the surface. The rupture plane dips toward the southwest. Note that free-surface topography is only illustrated to help the reader identify the study region; it is not included in the simulations within this study. The color version of this figure is available only in the electronic edition.

background 1D-layered velocity model (for one choice of a random seed) using a vertical correlation length of 150 m, $H = 0.05$, and $\sigma = 5\%$, at a grid spacing of 20 m. Our 3D background velocity models are extracted from the CVM-SI4.26 (Lee and Chen, 2014), in which the 3D long-wavelength velocity structure of the Los Angeles basin is relatively well known. Because the rupture does not reach the surface, there is negligible effect on the moment magnitude of each event; the variations in the rigidity at depth average out to give the same magnitude to that used in the 1D-layered velocity model. In geotechnical engineering, it is generally accepted that a large part of ground shaking is related to upward propagating body waves, due to the bending of seismic rays toward the surface. We ran tests with and without a GTL and found that the GTL significantly increased the ground motion outside valleys and basins with respect to the original CVM-SI4.26, due to the reduction in otherwise unrealistically high velocities in the background CVM. Figure 7 plots the shear-wave structure at 100 m depth with and without the superposition of small-scale media heterogeneity using the CVM-SI4.26 with the GTL. We set the minimum shear velocity to 500 m/s, which limits the highest resolved frequency to 5 Hz in our 3D models. We fix the velocities after superimposing small-scale heterogeneity to retain the broadest possible frequency content throughout the bulk of the medium; this introduces a small bias in the shear-wave velocity in the lowest velocity regions of Figure 7, allowing only positive variations in small-scale heterogeneity near the surface (typically only the top 1–2 grid points).

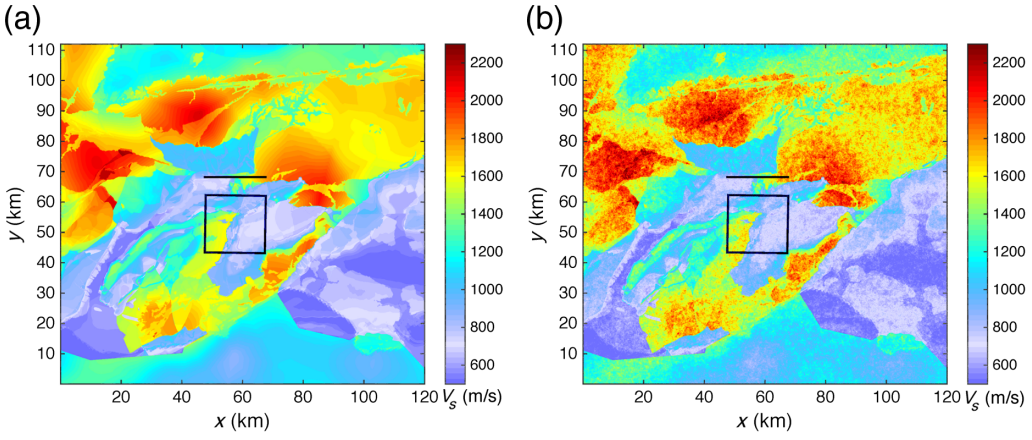


**Figure 7.** Map view of the shear-wave velocity extracted from the Community Velocity Model (CVM; CVM-SI4.26) at 100-m depth, including a geotechnical layer (GTL) layer (a) without and (b) with small-scale media heterogeneity. Note the change in the coordinate system from the dynamic rupture simulations. The rectangle and line depict the vertical projection and the intersection of the fault plane at the surface, respectively. The color version of this figure is available only in the electronic edition.

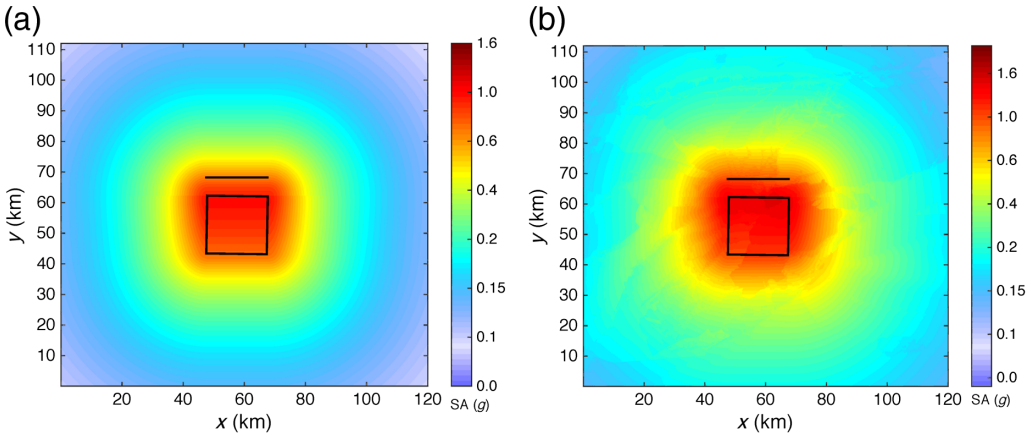


**Figure 8.** Average of four ground-motion prediction equation media predictions of spectral acceleration (SA)($g$) at a period of 0.3 s (a) for a 1D-layered model and (b) CVM-SI4.26, including a GTL layer. The rectangle and line depict the vertical projection and the intersection of the fault plane at the surface, respectively. The color version of this figure is available only in the electronic edition.

In addition to complex anelastic attenuation structure, we model nonlinearity effects from plasticity, omitted within the dynamic rupture simulations. Roten *et al.* (2012) demonstrated that the overprediction of near-fault GMPE values in simulations along the San Andreas is largely eliminated after a correction of the broadband synthetics for nonlinear soil effects is applied, reducing spectral accelerations (SAs) from viscoelastic simulations by up to 70%. Recent simulations of the ShakeOut scenario for an elasto-plastic medium predict long-period ground motions that are 30%–70% lower compared to viscoelastic solutions in the Los Angeles basin (Roten *et al.*, 2014). We combined our $Q(f)$ wave-propagation code (Withers *et al.*, 2015) with that of a medium governed by Drucker–Prager plasticity (Roten *et al.*, 2014) to implement viscoelastoplasticity, in which yielding occurs in shear via a return-map algorithm. The off-fault material responds elastically until stresses exceed a Drucker–Prager yield condition, after which viscoplastic deformation occurs. We included plasticity within some simulations, assuming a north-northeast–south-southwest direction of the major principal stress for computation of the initial stress tensor (representative of regional stress fields in central and southern California (Flesch *et al.*, 2000; Townend and Zoback, 2004) and hydrostatic fluid pressure at all depths. This approach uses the Hoek–Brown criterion for rock fracture based on the geological strength index (Hoek and Brown, 1997), with the cohesion and friction angle values set to values typical of a sandstone (see Roten *et al.*, 2017 for more details of this approach). We store the quantity $\eta$ at the final timestep in our simulations, which represents the accumulated inelastic strain due to yielding. This parameter allows determination of the regions that have been most strongly affected by plasticity.

## Results

We assess the validity of the synthetic ground motion by first comparing SA (as a function of period) and cumulative absolute velocity (CAV) with that of GMPEs derived from empirical observations. Next, we analyze simple proxy metrics that highlight the significance of media complexity with variation in period. Finally, even though our simulations are not designed to fit the specific slip asperities of the Northridge earthquake (only rupture size and initial stress conditions control the rupture propagation), we investigate how our ground-motion simulations compare with observed strong ground motion records.

### Spectral Acceleration

We compute median SA (using GMRotD50; Boore, 2006) and variability from four recent NGA-West2 relations (Abrahamson *et al.*, 2014; Campbell and Bozorgnia, 2014; Chiou and Youngs, 2014; Boore *et al.*, 2015) for both the 1D-layered and 3D background media. The most important factor (aside from magnitude) controlling the amount of strong shaking in an event is the distance from the site to the fault plane. Different GMPE models rely on one or more parameters to describe distance: $R_{\text{rup}}$, the closest distance to rupture plane; $R_x$, the horizontal distance to the top of the rupture perpendicular to strike; and $R_{\text{JB}}$, the Joyner–Boore [JB] distance, the horizontal distance to the surface projection of the rupture. We calculate these and other parameters needed for the GMPE relations for an 80-m grid at the surface (corresponding to every fourth node of our computational mesh). The average of the four GMPEs for SA at a period of 0.3 s is plotted in Figure 8 for the 1D-layered model and CVM (using the local values of $Z_{1.0}$, $Z_{2.5}$, and $V_{S30}$ used in the simulation to compute the GMPE prediction). The Boore *et al.* (2015) model is only dependent on the JB distance and thus predicts invariant ground motion at a constant distance from the surface projection of the fault plane. The other GMPE models are dependent on $R_{\text{rup}}$ and $R_x$ (in addition to $R_{\text{JB}}$), creating more asymmetric patterns of ground motion, with larger response toward the up-dip region of the fault plane.

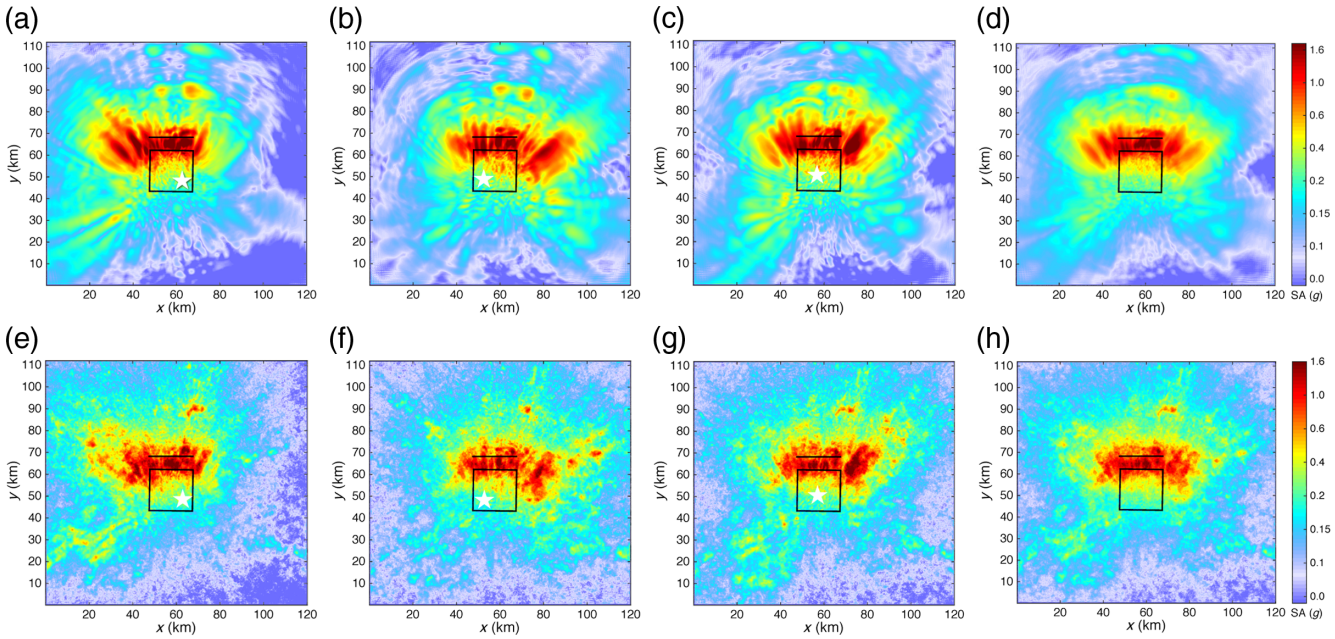


**Figure 9.** SA($g$) at $T = 0.3$ s for (a–d) models without small-scale heterogeneity and (e–h) including small-scale heterogeneity. (a–c) and (d–f) indicate the three epicenter locations (by stars) depicted in Figure 3, corresponding to events 1–3, with (d,h) the average of (a–c) and (d–f), respectively. The rectangle and line depict the vertical projection and the intersection of the fault plane at the surface, respectively. The color version of this figure is available only in the electronic edition.

Figure 9 plots SA at 0.3 s period for events 1–3 and their average, using the 1D-layered model in our simulations. We include small-scale media heterogeneity with a vertical correlation length of 150 m, a Hurst exponent of 0.05, a horizontal-to-vertical stretching factor or 5 (for the remainder of this article, correlation length refers to the vertical correlation length, with a stretching factor of 5 used in the horizontal dimension), and a standard deviation of the medium variations of $\sigma = 5\%$ (within the range observed in southern California, e.g., Nakata and Beroza, 2015; Savran and Olsen, 2016). Anelastic attenuation is implemented according to Withers *et al.* (2018) with $Q(f) = Q_0 f^{\gamma}$ and a transition frequency of 1 Hz, in which $Q_{S0} = V_S \times 0.05$ and $Q_{P0} = 2 \times Q_{S0}$, in which $V_S$ is in m/s and $\gamma = 0.8$.

The synthetic ground motion in Figure 9 has a similar range in amplitude to that of GMPEs (Fig. 8) but with a characteristically different spatial pattern. For example, ground motion from all three events has a pronounced peak near the intersection of the projection of the fault plane to the free surface (with the largest ground motion located on the opposite side of the fault plane from that of the epicenter location). This feature is likely due to the hypocentral locations being at depth and the lack of a 3D long-wavelength structure that may help break up directivity at HFs (this latter hypothesis is later analyzed further, as a function of $R_x$). Furthermore, there are concentric rings and radiating streaks present for models without small-scale heterogeneity (Fig. 9a–d). These features are likely due to the simplified velocity structure, because they are independent of hypocenter location, possibly from energy reverberating in the shallow-velocity layers near the free surface, similar to a waveguide effect.

Averaging the three models smooths out some of the variation observed in the spatial patterns. Small-scale heterogeneity serves to redistribute energy at the local scale, in contrast to that observed for a bilateral strike-slip event in the companion paper (Withers *et al.*, 2018). This difference is due to the style of faulting, in which energy is distributed in lobes oriented near the dipping plane of the fault, disallowing significant spatial variation in the ground-motion pattern at the surface. Additionally, the shorter path length from source to receivers reduces the role of scattering.

We group stations as a function of $R_{\text{rup}}$ and plot median SA at three distance bins (1-km width) within our model domain in Figure 10. The average $\pm 1$ interevent standard deviations are added to the range of the four GMPEs' median ground motion (computed using $M_{\text{w}} = 6.76$, and the local distance, velocity, and depth parameters, e.g., $Z_{1.0}$, $Z_{2.5}$, and $V_{S30}$). We choose to use the $R_{\text{rup}}$ distance because it allows for more variability near the fault than the $R_{\text{JB}}$ distance, symmetric about the projection to the surface of the fault rupture plane with large areas of zero value. The simulated SAs are within one standard deviation of that predicted by the NGA relations and generally lie within the 50th percentile range of the GMPEs (the shaded region in each graph). The anelastic power-law exponent of 0.8 above 1 Hz produces trends comparable with the GMPEs' ground motion versus both period and distance. The median ground motion varies little for the three events and is almost independent of small-scale media heterogeneity (across varying correlation lengths);

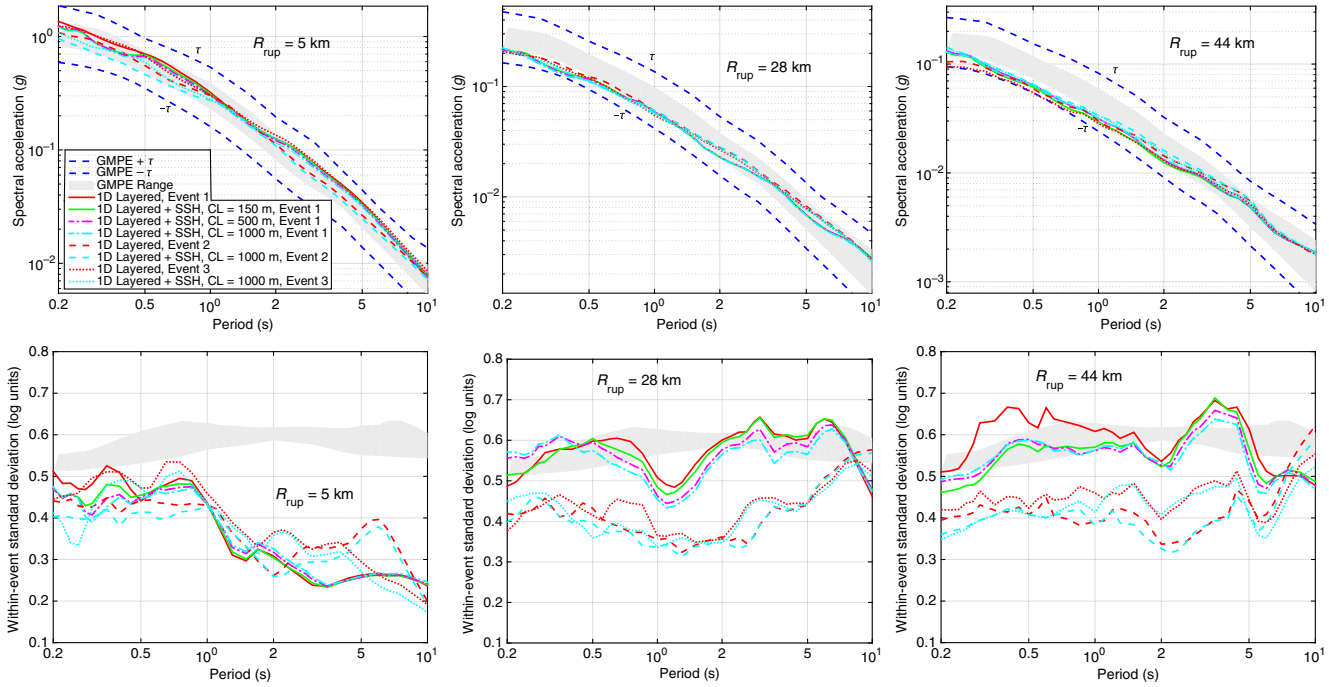


**Figure 10.** Median SA and intraevent variability as a function of period at a short, medium, and far distance (within our model domain). SSH, small-scale heterogeneity; CL, correlation length. The color version of this figure is available only in the electronic edition.

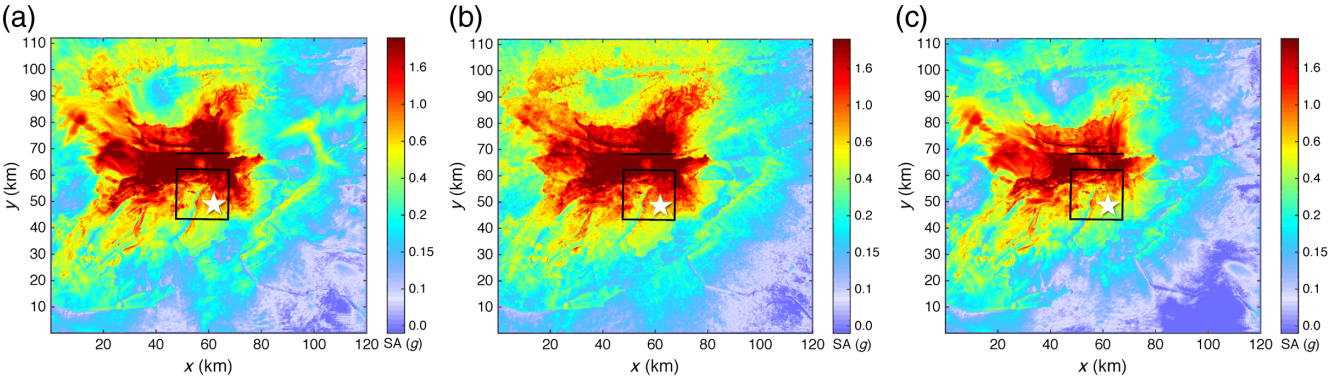


**Figure 11.** SA at 0.3 s (*g*) for a background 3D model (a) without small-scale heterogeneity, (b) including small-scale heterogeneity, and (c) including both plasticity and small-scale heterogeneity. The rectangle and line depict the vertical projection and the intersection of the fault plane at the surface, respectively, whereas the star depicts the epicentral location. The color version of this figure is available only in the electronic edition.

the spatial variations that are present in Figure 9 are lost when binning stations as a function of distance.

The corresponding intraevent (or within-event, used interchangeably throughout the article) variability is also plotted in Figure 10, showing similar standard deviations for all models with a small $R_{rup}$, with larger deviations at farther distances. At larger distances, event 1 has variability very near that of the GMPE-predicted range, with only a slight reduction when small-scale heterogeneity is included (most significant above 1 Hz). Events 2 and 3 have lower variability than event 1 and the empirical observations across the entire bandwidth. This is due to the spatial patterns observed in Figure 9; events 2 and 3 have a more equal azimuthal distribution of ground motion as compared to event 1 that has reduced ground motion on the right side of the model domain (likely attributed to the reduced slip rates along that side of the fault, as seen in Fig. 3). Thus, the averaged intraevent variability from the three simulations is slightly lower than that predicted by the GMPEs. This may be due to the simplified 1D background-layered velocity structure, for which we might expect similar values to that of single-station standard deviation values, because there is no variation in the site component, previously shown to be ~10% smaller than that modeled from GMPEs (Atkinson, 2006; Rodriguez-Marek *et al.*, 2013).

Next, we compare ground motion with a 3D background velocity model. Figure 11 plots SA at 0.3 s for event 1, with

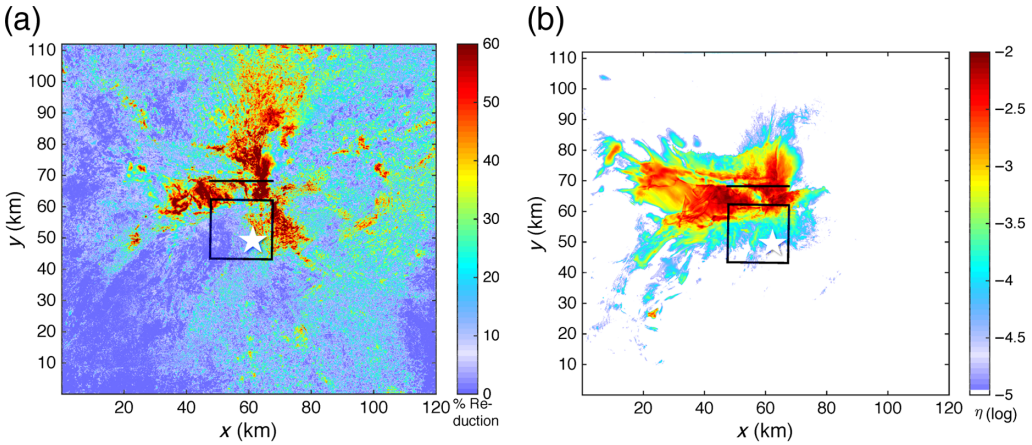


**Figure 12.** (a) Reduction of SA (%) at 0.3 s for event 1 when including plasticity using a background CVM. (b) Final principal plastic strain $\eta$ at the surface (log units). The rectangle and line depict the vertical projection and the intersection of the fault plane at the surface, respectively, whereas the star depicts the epicentral location. The color version of this figure is available only in the electronic edition.

and without small-scale media heterogeneity, and a simulation including plasticity. A more complex pattern of ground motion is generated from the CVM background structure compared to the 1D-layered model, due to additional scattering that redistributes the seismic energy and site effects. Source directivity is evident but is obscured by what is likely basin-edge amplification that increases ground motions in the left region of the model domain. Small-scale heterogeneity smears out coherent features along narrow spatial domains (such as distinct energy bands), whereas plasticity reduces ground motion over large regions. Figure 12 plots this reduction in ground-motion amplitude from nonlinearity, reaching as high as 70% in some areas (the scale bar in the figure is saturated at 60%). The regions most affected are located mainly near the surface projection of the fault, but a large lobe also exists extending along the footwall. Figure 12 plots the spatial pattern of total accumulated inelastic strain generated by this rupture event. Even though there is still a significant reduction in ground motion at 30–40 km from the fault, there is little or no permanent plastic strain accumulation in these regions, indicating that nonlinear effects can cause significant reduction in ground motion at distances beyond regions directly affected by permanent deformation, as shown previously by Roten *et al.* (2014).

Figure 13 plots ground motion and its variability for stations located within basins, defined as where the depth to $Z_{1.0}$ (the depth where $V_S$ reaches 1 km/s) is less than 100 m (with all other parameters, e.g., $Z_{2.5}$, and $V_{S30}$, as used in the simulation, as in Fig. 8b). This choice of velocity produces a spatial pattern with more basin stations located on the HW than the footwall (see Fig. 7 for the location of rock site and basins). To remove any potential spatial bias, we extract a subset of receivers by randomly selecting an equal number of stations for both negative and positive $R_x$ (this required expanding the width of our bins from 1 to 6 km to have a sufficient number of stations for analysis). We are only able to resolve ground motion up to a frequency of 5 Hz in these 3D models, due to the accuracy of our AWP finite-difference algorithm (based on 5 points per wavelength, with the minimum shear-wave velocity in our model, 500 m/s).

Median ground motion follows a similar trend to that of the GMPEs, with small-scale heterogeneity playing a relatively minor role. The biggest difference between models occurs at small $R_{rup}$, particularly at shorter periods, during which nonlinear effects reduce the ground motion, but still lying near the range of the median GMPEs. The intraevent standard deviation in the 3D models has similar characteristics to that observed in the 1D-layered models: the variability near the fault decreases while progressing from short to long periods, with levels at periods larger than 1 s within 0.1–0.2 logarithmic units below the GMPE range. The standard deviation is significantly reduced in regions (and bandwidth) where ground motion is reduced by nonlinearity.

The corresponding ground motion and its variability for rock sites (defined as $Z_{1.0} > 100$ m) is plotted in Figure 14. We note that there are not large variations in the levels of the GMPEs in the rock versus basin sites (as seen in Fig. 8); in some cases, the ground motion is almost identical. There would likely be larger contrasts if we incorporated lower velocities in the near surface (which we chose to avoid here to maintain accuracy at HFs within our simulations), allowing for increased amplification. Median ground-motion levels again generally follow the trend of the GMPE medians; plasticity has a significant effect at shorter periods, decreasing amplitudes at the short and moderate distances into the range of the GMPE medians but below that at the farthest distances. As discussed later, additional models incorporating plasticity should be performed to understand the influence of the choice of nonlinear parameters. As seen for basin sites, variability tends to decrease as period increases, starting at a quite large value at the short and intermediate distances, where source effects have more of an impact than at larger $R_{rup}$.

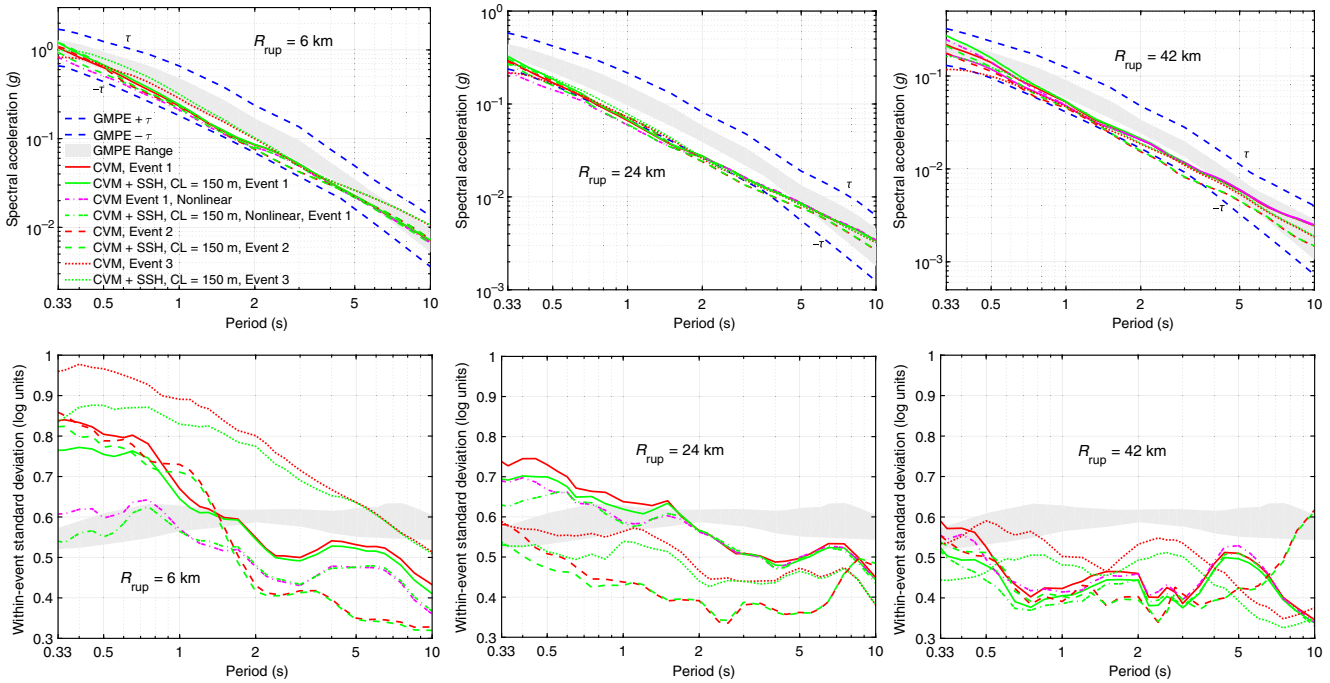


**Figure 13.** Similar to Figure 10, but using a 3D model with stations located in the basin. The color version of this figure is available only in the electronic edition.

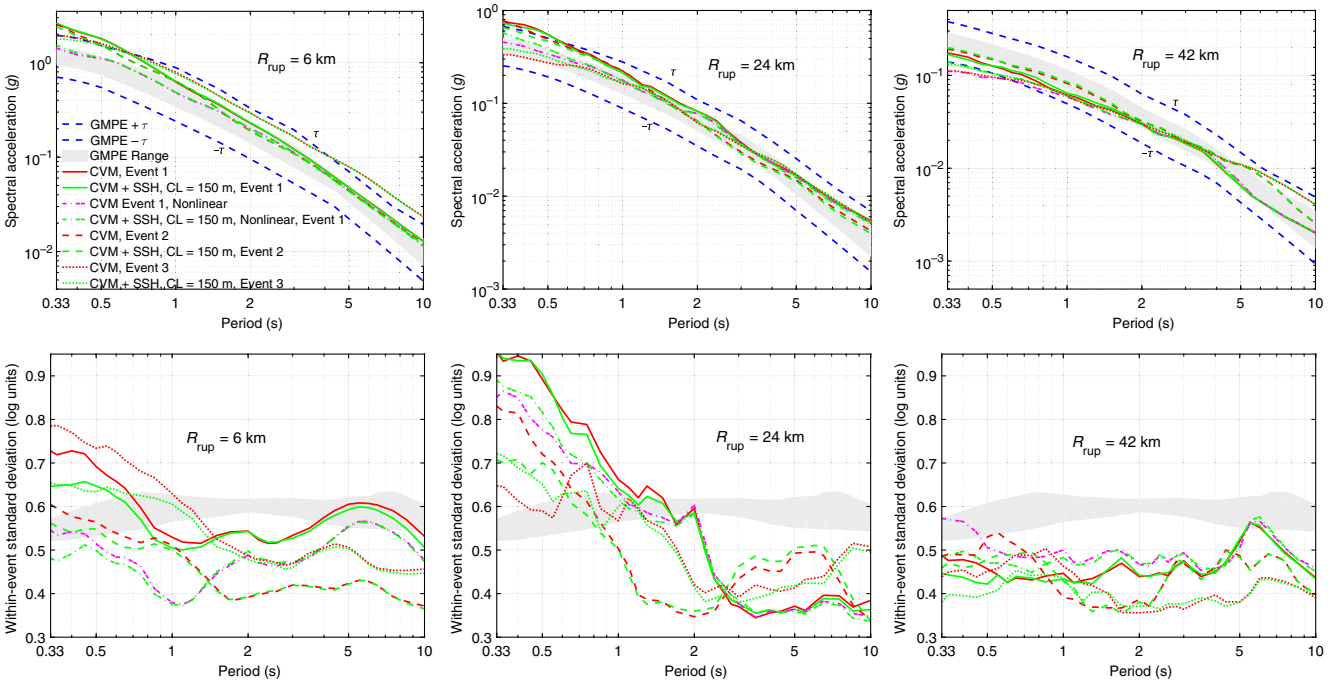


**Figure 14.** Similar to Figure 13, but for rock sites. The color version of this figure is available only in the electronic edition.

## Cumulative Absolute Velocity

Analyzing ground motion with metrics complementary to those based on peak motions can illuminate additional aspects of our simulations. One example is the CAV, defined as the integral of the absolute value of the acceleration time series. Campbell and Bozorgnia (2012) developed a GMPE for both Arias intensity ($I_A$) and CAV, based on their previous 2008 GMPE model form, taking into account amplification due to basin structure. CAV includes the cumulative effects of ground-motion duration and has smaller intraevent variabil-

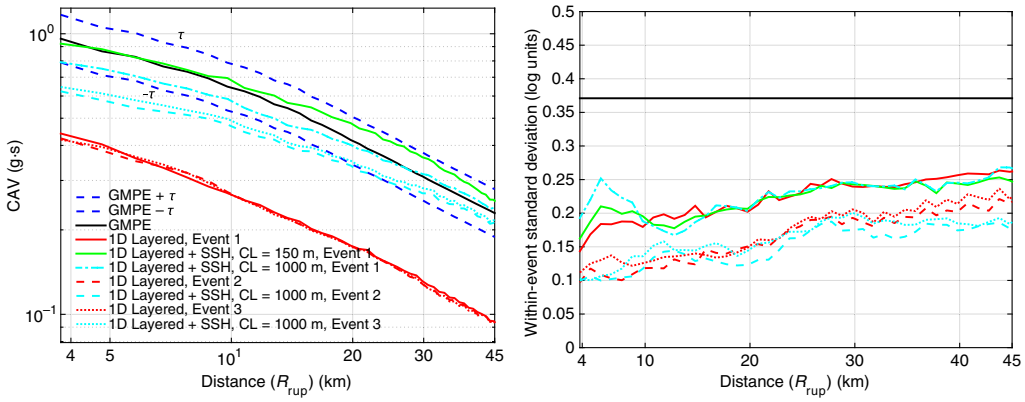


**Figure 15.** Cumulative absolute velocity (CAV) and its intraevent variability versus distance for 1D-layered velocity models. The color version of this figure is available only in the electronic edition.

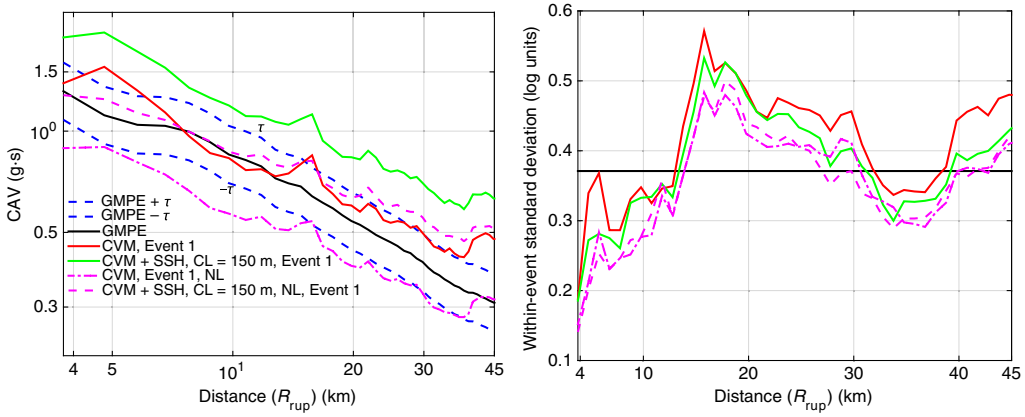


**Figure 16.** CAV and its intraevent variability versus distance at basin sites using a background CVM. NL, nonlinearity from plasticity. The color version of this figure is available only in the electronic edition.

ity than $I_A$, due to the difference in the square rather than absolute value of acceleration, thus having a higher predictability (Campbell and Bozorgnia, 2010). The geometric mean of the orthogonal horizontal components is computed from the synthetic data and compared with that of the Campbell and Bozorgnia (2012) model. Figure 15 plots results for 1D-layered models. Models without small-scale heterogeneity underpredict the GMPE trend by over two interevent standard deviations. Scattering from small-scale heterogeneity increases the energy in the later parts of the time series at HFs, influencing acceleration, bringing the trend closer to that of the GMPE median. Shorter correlation lengths lead to larger median CAV, indicating the importance of scattering from wavelengths sensitive to small spatial structure. A correlation length of 150 m best matches the amplitude and trend of median ground motion seen in the GMPE. Intraevent variability is very similar for models with and without small-scale heterogeneity structure (and as with SA, is lower for events 2 and 3, compared to event 1). All three events have a trend that increases as a function of distance, at a level significantly below that derived from empirical observations.

Figures 16 and 17 show CAV for basin and rock sites, respectively (defined the same way as for SAs on $Z_{1.0}$ and using the values of $Z_{2.5}$ and $V_{S30}$ as used in the simulation). The 3D CVM structure significantly increases the median CAV, with small-scale heterogeneity increasing it further. Including plasticity decreases CAV, but incorporating both plasticity and small-scale heterogeneity best matches the predicted decay in CAV as a function of distance for the parameters used here. There are no large clear, systematic differences in the intraevent variability; it fluctuates near the GMPE range for basin sites, while being event dependent for rock sites (see Ⓔ Figs. S5 and S6, for events 2 and 3).

### $SA_{RotD100}/SA_{RotD50}$

A group of proxy metrics is outlined in Burks and Baker (2014) that are relatively stable, having little variation across a range of tectonic regimes, magnitude, distance, and site conditions. One of these is $SA_{RotD100}/SA_{RotD50}$, the ratio of maximum to median SA across orientations, calculated as a function of period. This metric is a measure of the amplitude

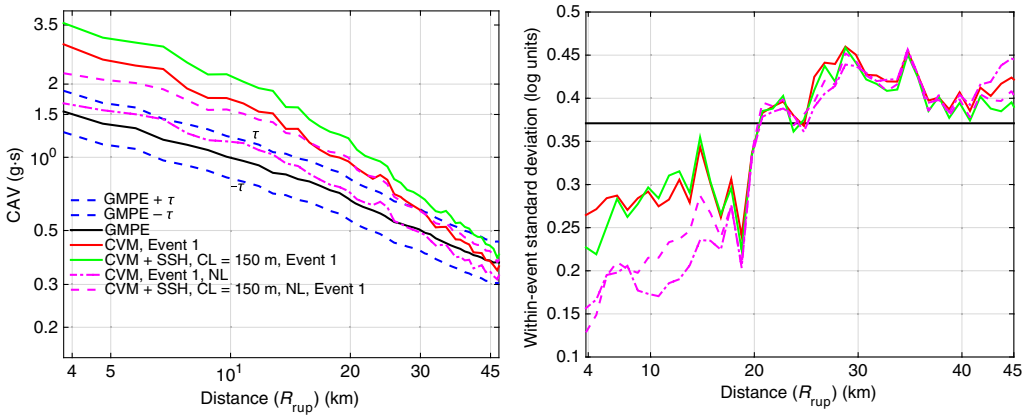


**Figure 17.** Same as Figure 16 but for rock sites. The color version of this figure is available only in the electronic edition.

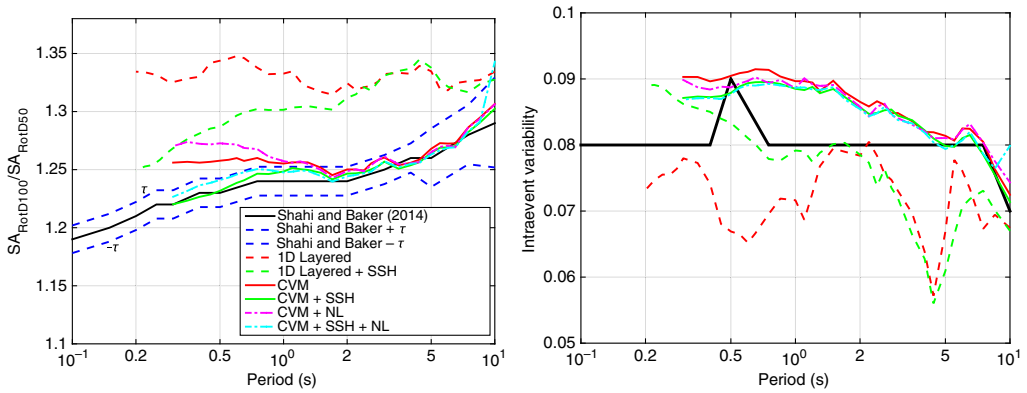


**Figure 18.** $SA_{RotD100}/SA_{RotD50}$ and intraevent variability for various synthetic models compared with the Shahi and Baker (2014) model prediction. The color version of this figure is available only in the electronic edition.

polarization and is consistent across both dip-slip and strike-slip earthquakes.

Figure 18 plots both $SA_{RotD100}/SA_{RotD50}$ and intraevent variability from event 1, in addition to the empirical model from Shahi and Baker (2014). The results here are consistent across multiple source models, showing little variation across the three events used in this study. The median for 1D-layered models is roughly constant, near a ratio of 1.32 for the bandwidth studied here, much higher than the Shahi and Baker (2014) model. Including small-scale heterogeneity significantly reduces the short-period ($< 2$ s) median but remains much larger than that of empirical observations. A CVM background structure, however, reduces the 2–10 s period range to that expected from empirical data. Small-scale heterogeneity (with a correlation length of 150 m) further reduces the shorter period medians into the expected range as well, indicating that both small-scale and large-scale media variation in deterministic models are needed in simulations to match this proxy metric. We ran additional 1D-layered simulations (not plotted) and found that a correlation length of 1000 m did not significantly reduce the ratio at longer periods, as the 3D model does. The sharp velocity contrasts in the CVM redistribute energy more randomly at long wavelengths than the gradual changes in small-scale heterogeneity, causing the waves to be more equally polarized (in the horizontal components), reducing the ratio. Plasticity decreases the fit to data at the shortest periods, but still lies near the expected range when small-scale heterogeneity is included. The variability from CVM simulations is near that of the GMPE, with little variation among models, whereas the 1D-layered models tend to have slightly lower variability than that expected from observations.

### $\epsilon$ (Period-to-Period Correlation of SA)

Another proxy metric is $\epsilon$, the correlation of SA residuals at varying periods. $\epsilon$ is defined as the normalized difference between an observed SA and the mean predicted natural log of SA from a GMPE. Baker and Jayaram (2008) examined SA values at multiple periods and orientations. They fit the NGA ground-motion database for $\epsilon(T)$, using the Pearson product-moment correlation coefficient, finding that intraevent residuals have essentially identical correlation structure to the total residuals. This correlation $\rho$ is related to the width of peaks and troughs in the spectra and has been

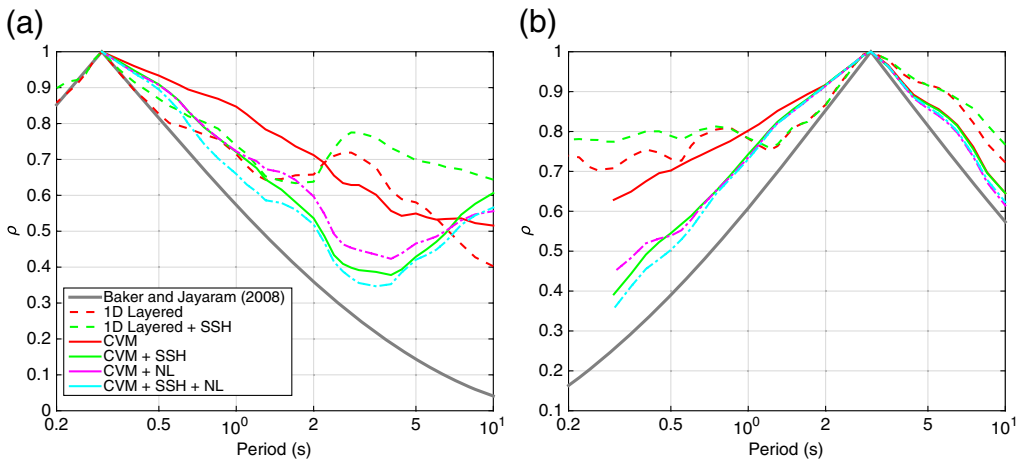


**Figure 19.** Correlation of $\epsilon$ at a reference period of (a) 0.3 and (b) 3 s from simulations compared with Baker and Jayaram (2008). The color version of this figure is available only in the electronic edition.

shown to be stable for varying reference GMPEs in the 0.3–10 Hz frequency range (Baker and Jayaram, 2008).

Figure 19 plots $\rho$, the correlation across periods, for one long reference period of 3 s and one short reference period of 0.3 s. The correlation in a narrow bandwidth near the reference period is near that of observations. As frequency increases away from the reference frequency, however, 1D-layered models have a significantly larger correlation than observations. Simulations with a background CVM increase $\rho$ near the reference period but have smaller $\rho$ at periods farther from the reference period, closer to the Baker and Jayaram (2008) model. A large reduction in correlation at shorter periods occurs in models that include small-scale heterogeneity; the random velocity structure serves to rid neighboring frequencies of high correlation. At a short reference period, there is an upward trend in correlation, starting near 3 s in 3D models with small-scale heterogeneity. This may be due to the overlap of deterministic and stochastic structure, indicating that this transition needs to be more carefully defined. The correlation would likely be reduced if lower velocities were included in the CVM simulations, allowing more variation in the shear-wave velocity in the near surface.

## Bias

We compare our synthetic results with that of observed ground motions from the Northridge event. This was a particularly well-recorded earthquake with near-field stations on both hard-rock and soft-soil sites, including stations that experienced de-amplification from nonlinear effects. The ground motion was large, particularly in regions experiencing directivity (up-dip toward the north), with ground accelerations being some of the highest ever instrumentally recorded in an urban area of North America (up to 1.8$g$). Even though our simulation was not designed to match the Northridge earthquake specifically, there are similarities that make it useful to compare the synthetics with recorded strong-motion data. We used a scaling factor of 1.34 to decrease event 1's magnitude ($M_w \sim 6.76$) to that of the estimated moment of the Northridge earthquake ($M_w \sim 6.7$) and calculate the pseudo-spectral acceleration bias (ln[data/model]) versus period for stations located within our model region (see Fig. 6). For the 1D-layered models, we use the response spectra from Goulet *et al.* (2015), corrected for a $V_{S30}$ of 863 m/s (using the adjustment factors from Boore *et al.*, 2015) and the basin effects model of Chiou and Youngs (2008). To compare with the CVM simulation, we first compute response spectra and adjust only for site effects (to a $V_{S30}$ near 863 m/s), using equations (6) and (7) in Boore *et al.* (2015) corresponding to the linear and nonlinear term, respectively). This keeps the basin term in the response spectra, allowing for direct comparison with the CVM simulation.

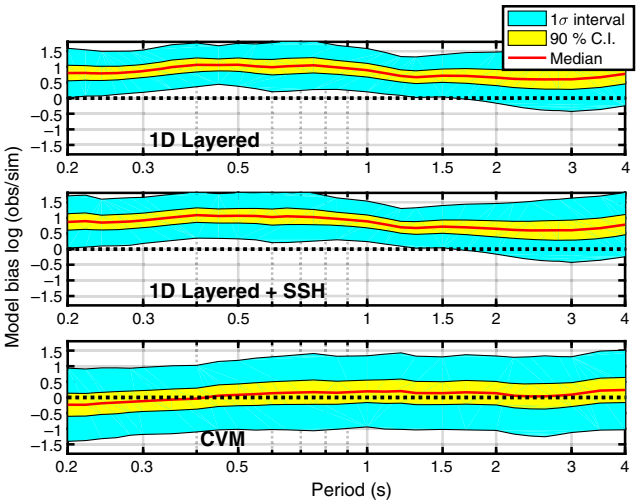


**Figure 20.** Bias (ln[data/model]) of SA, depicting median, 95% confidence interval, and standard deviation. The color version of this figure is available only in the electronic edition.

Figure 20 plots the bias, depicting the median, 95% confidence interval, and standard deviation for both 1D-layered and CVM simulations (here, we compare with an additional

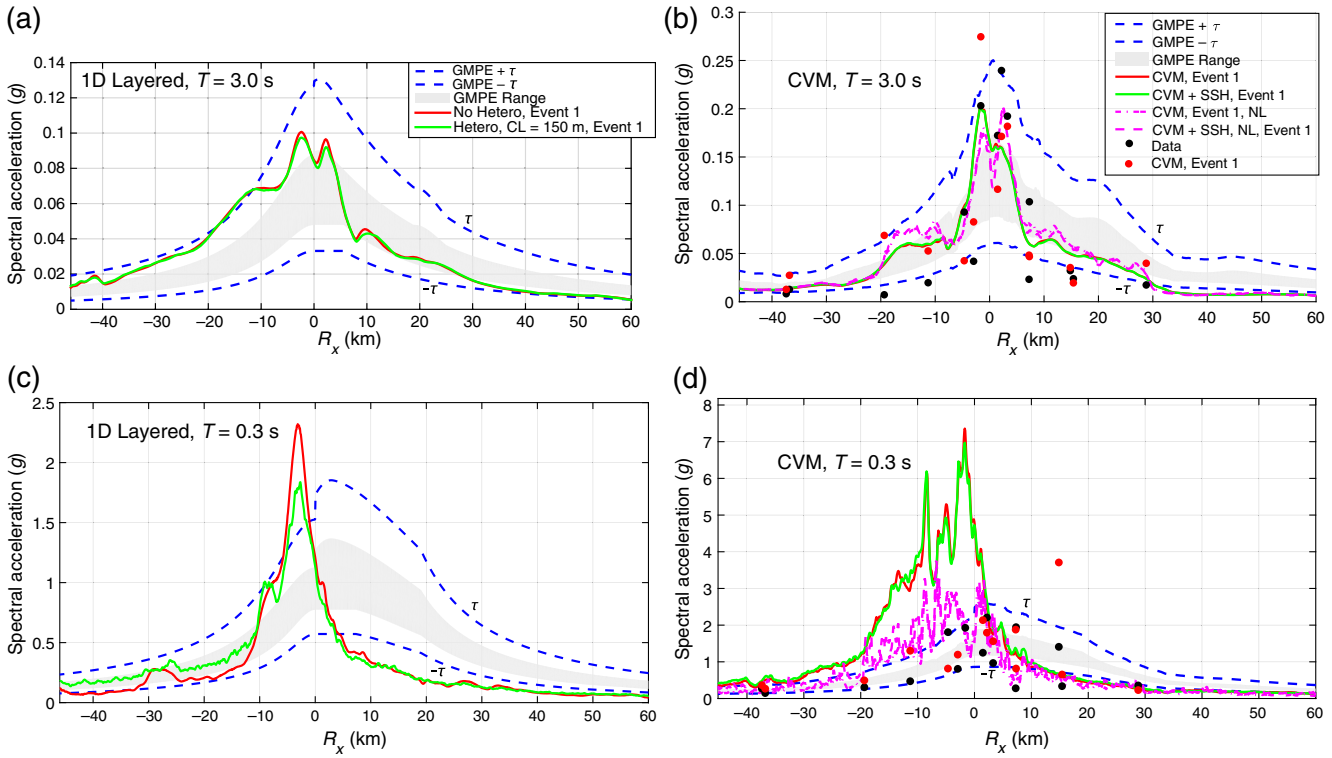


**Figure 21.** SA ($g$) versus $R_x$ for averaged profiles within the fault strike, for (a,c) 1D-layered models, and (b,d) 3D CVM structures. (a,b) are for periods of 3.0 s and (c,d) for 0.3 s. Events 2 and 3 are excluded to retain image clarity. The color version of this figure is available only in the electronic edition.

CVM simulation with a minimum $S$-wave velocity of 863 m/s, as opposed to 500 m/s, for a more direct comparison with the 1D-layered simulations and to maintain the computational accuracy at the higher frequencies). 1D-layered models have positive residuals across all periods, indicating that an underprediction with respect to the empirical data. Small-scale heterogeneity has little effect, but the background CVM structure reduces bias considerably, causing the zero-bias level to lie within or near the $\pm 1\sigma$ interval of the recorded motions. This potentially has important implications for the limitation of using 1D-layered velocity models when modeling specific earthquakes. We do not include plasticity in any of these models because we effectively (by clamping) use a hard-rock velocity profile in which nonlinear effects should not be significant.

### $R_x$ Dependence

We study an aspect commonly observed in dip-slip earthquakes, namely the hanging-wall (HW) effect, where there is increased ground motion on the HW side of the rupture compared to the footwall (Donahue and Abrahamson, 2014). This is mainly a geometrical effect, due to the closest distance metric and present in seismic records from the 1994 Northridge earthquake (Abrahamson and Somerville, 1996). Figure 21 plots GMPEs and synthetic data at a low and HF SA along a cross section perpendicular to strike, averaged along profiles lying within the fault strike ($R_{y0} = 0$) for event 1 (see Ⓔ Fig. S7, for events 2 and 3). We use $R_x$, the horizontal distance from the top of the rupture to the site, as the distance parameter (with positive values of $R_x$ defined as on the HW side). The HW effect reaches the maximum value over the bottom edge of the rupture. The ground motion in Figure 21 predicted by GMPEs is sightly larger on the HW for both LFs and HFs, compared to the equivalent distances on the footwall (being more pronounced at shorter periods).

The 1D-layered synthetics lie within the GMPE bounds ($\pm 1\tau$ or interevent standard deviation) at 3 s, with significant variation between events. Event 2 has the clearest indication of a HW effect, but this characteristic vanishes when looking at 0.3 s, at which all events have a large peak in the $R_x = -5$ and 0-km range, where the ground motion is focused from the dipping fault plane to the free surface. This peak is averaged out when looking at ground motion as a function of $R_{\text{rup}}$ because it is balanced by much lower median ground motion for positive $R_x$ in this distance range.

Simulations with a background CVM have similar behavior to 1D models but with a significant reduction in ground motion from plasticity at HF. For comparison, we also include the recorded data for stations with $R_{y0} = 0$ and the corresponding synthetic value (using the 3D model, event 1), both corrected to a $V_{S30}$ of 863 m/s to minimize any variation caused by site effects (thus only the trend of SA with $R_x$ at specific stations should be analyzed in this plot, not absolute values). We do not observe a clear trend with the few data points plotted here.

In summary, a HW effect is not evident in the 1D-layered simulations; this may be due to directivity obscuring the amplification pattern, overpowering any geometric effect. Simulations with the CVM also have strong directivity, likely additionally obscuring the HW effect from complex reverberations in the basin. However, further simulations that more fully explore the parameter space (particularly in the source) run in both a 1D-layered and CVM are warranted to better support these hypotheses.

## Discussion and Conclusions

GMPEs provide the foundation on which seismic design and construction of the built environments rests, as well as seismic safety. There are sparse ground-motion data for $M_w > 6.7$ earthquakes on reverse faults. To supplement empirical observations, simulations provide an approach to study certain features that may rarely be observed, due to lack of data and spatial coverage. Before simulations can be used for engineering applications, validation is required to demonstrate that simulations have similar characteristics to observed ground motions. This requires that simulations agree with pre-existing relations, in terms of both their median and variability behavior and as a function of distance and frequency.

Here, we modeled broadband ground motion along buried dip-slip events with fault-surface roughness. We compared ground motions experienced in both 1D-layered and 3D background models, including features such as small-scale media heterogeneity, plasticity via the Drucker–Prager yield condition, and frequency-dependent attenuation. We found that the synthetic SA, at various periods, matches the distance decay of GMPEs. Although the ground-motion pattern changes, the spatially averaged median SA is not significantly affected by small-scale media heterogeneity, and intraevent variability is fairly independent of correlation length. However, small-scale heterogeneity serves to significantly increase the CAV, bringing it closer to that of GMPEs, particularly in 1D-layered models, indicating that scattering is needed to match metrics dependent on duration. We found that unconsolidated deposits may significantly amplify the ground motion during a large earthquake, especially at frequencies >1 Hz; ignoring nonlinear effects might result in costly misguidance in earthquake-prone regions. Additionally, we compare several proxy metrics with our simulations and find that 3D heterogeneity at both long- and short-scale lengths is necessary to agree with observations. Specifically, small-scale media heterogeneity decreases the polarization ratio and the correlation across periods to values closer to those for observations, indicating the importance of including stochastic-based media heterogeneity as ground-motion prediction extends to higher frequencies.

The simulations along the blind-thrust fault here represent only a small subset of potential rupture scenarios and velocity structures that need to be examined to more fully vet our approach. We found similar trends with period for the three events used here, as expected because they share similar slip distributions, common rupture areas, rupture speeds, and rise times. Even so, it is shown that ground motion is strongly influenced by source parameters (such as the hypocenter location); additional simulations should explore the extent of predictability of strong ground motion for both specific and generic events. For example, dynamic parameters (such as dynamic and static frictional coefficients) would alter the rupture velocity as well as stress drop, creating varying ground-motion patterns related directly to the source. We used only one choice of parameters for nonlinearity in this article; Roten *et al.* (2014) performed a more thorough parameter space study, with varying plasticity coefficients, and found that cohesion has a large impact on the resulting ground motion. Our single parameterization is in the middle of the range of expected impact from plasticity and emphasizes situations in which plasticity is important. Future investigations with models including nonlinearity should be performed to further understand the range of possible behavior but will likely not change any of the conclusions found here.

The interevent standard deviation of ground motion from the ensemble of earthquakes with different hypocenter locations is small but is expected to increase when using varying rough-fault topographies and a more distributed set of hypocenter locations. Presumably, if a suite of simulations was performed with hypocentral locations distributed more uniformly along the fault, the average ground-motion pattern would be similar to that predicted from GMPEs (as shown in Fig. 8).

Abrahamson and Somerville (1996) used the Northridge event as one of the main contributors for including terms for HW effects in the GMPEs. Our study, however, did not find any clear dependence on ground motion related to the HW effect, that is, amplified ground motion for positive $R_x$. This may be partially due to the rupture being a blind event; the HW effect is known to be de-amplified for ruptures not reaching the surface (Donahue and Abrahamson, 2014). Indeed, we find strongly amplified ground motion near the location of the fault projected up-dip to the free surface, presumably due to directivity. However, this pronounced, relatively narrow, peak in SA was the strongest at shorter periods, in which the HW effect is expected to be the strongest. Another possibility that may explain the lack of asymmetric ground motion across the HW may be related to the velocity model. Here, we used a long-wavelength representation of the regional velocity model and superimposed a stochastic small-scale heterogeneous velocity model. Fine-tuning the transition wavelength in which each model has power (in the spatial domain) may help reduce the effect of directivity (by increased scattering), particularly at higher frequencies, creating more emphasis on secondary features such as the HW effect. Thus, further investigation is needed to reconcile the differences between the synthetic and observed ground motions for the Northridge earthquake.

We excluded the $\kappa_0$ (the site component of the spectral decay seen in ground-motion observations known as $\kappa$) technique we introduced in the companion paper (Withers *et al.*, 2018) for the simulations performed in this study. That approach introduced a shallow near-surface frequency-independent low-$Q$ layer to modify the HF energy decay that relates to $\kappa$. As discussed in that article, this approach serves to reduce the HF energy. This will likely not change the conclusions found in this article, either for GMPE comparisons or proxy metrics, because we are limited by computational constraints to 7.5 and 5 Hz in the 1D-layered and 3D models, respectively.

## Data and Resources

The southern California velocity model CVM-S 4.26 can be obtained from Southern California Earthquake Center (SCEC) at http://scec.usc.edu/scecpedia/. Most of the data-processing work was done using MATLAB (http://www.mathworks.com/products/matlab/). Figures were prepared using MATLAB and the Generic Mapping Tools package (http://www.soest.hawaii.edu/gmt/). All electronic addresses referenced here were last accessed on October 2017. The Northridge ground-motion data came from the SCEC Broadband Simulation Platform database (Goulet *et al.*, 2015). All other data used in this article came from published sources listed in the references.

## Acknowledgments

This research was supported through the Southern California Earthquake Center (SCEC) by the National Science Foundation (NSF) Cooperative Agreement EAR-0529922 and U.S. Geological Survey (USGS) Cooperative Agreement 07HQAG0008, by USGS Award G15AP00077, and by NSF Awards EAR-1135455, OCI-114849, EAR-1349180, and ACI-1450451. The simulations performed here were generated on the Titan Cray XK7 at the Oak Ridge Leadership Computing Facility in Tennessee. This is SCEC publication number 8071. The authors thank Associate Editor Adrian Rodriguez-Marek and reviewers Robert Graves and P. Martin Mai for comments contributing to an improved article. In addition, the authors are grateful to Brendon Bradley for helpful discussion and suggestions.

## References

Abrahamson, N. A., and P. G. Somerville (1996). Effects of the hanging wall and footwall on ground motions recorded during the Northridge earthquake, *Bull. Seismol. Soc. Am.* **86,** 93–99.

Abrahamson, N. A., W. J. Silva, and R. Kamai (2014). Summary of the ASK14 ground motion relation for active crustal regions, *Earthq. Spectra* **30,** 1025–1055.

Anderson, J. G. (2015). The composite source model for broadband simulations of strong ground motions, *Seismol. Res. Lett.* **86,** 68–74.

Atkinson, G. M. (2006). Single-station sigma, *Bull. Seismol. Soc. Am.* **96,** 446–455.

Atkinson, G. M., and K. Assatourians (2012). Implementation and validation of EXSIM (a stochastic finite-fault ground-motion simulation algorithm) on the SCEC broadband platform, *Seismol. Res. Lett.* **86,** 48–60.

Baker, J. W., and N. Jayaram (2008). Correlation of spectral acceleration values from NGA ground motion models, *Earthq. Spectra* **24,** 299–317.

Boore, D. M. (2006). Orientation-independent measures of ground motion, *Bull. Seismol. Soc. Am.* **96,** 1502–1511.

Boore, D. M., J. P. Stewart, E. Seyhan, and G. Atkinson (2015). NGA-West 2 equations for predicting PGA, PGV, and 5%-damped PSA for shallow crustal earthquakes, *Earthq. Spectra* **30,** 1057–1085.

Burks, L. S., and J. W. Baker (2014). Validation of ground-motion simulations through simple proxies for the response of engineered systems, *Bull. Seismol. Soc. Am.* **104,** 1930–1946.

Campbell, K. W., and Y. Bozorgnia (2010). A ground motion prediction equation for the horizontal component of cumulative absolute velocity (CAV) based on the PEER-NGA strong motion database, *Earthq. Spectra* **26,** 635–650.

Campbell, K. W., and Y. Bozorgnia (2012). A comparison of ground motion prediction equations for Arias intensity and cumulative absolute velocity developed using a consistent database and functional form, *Earthq. Spectra* **28,** 931–941.

Campbell, K. W., and Y. Bozorgnia (2014). NGA-West2 ground motion model for the average horizontal components of PGA, PGV, and 5%-damped linear acceleration response spectra, *Earthq. Spectra* **30,** 1087–1115.

Candela, T., F. Renard, Y. Klinger, K. Mair, J. Schmittbuhl, and E. E. Brodsky (2012). Roughness of fault surfaces over nine decades of length scales, *J. Geophys. Res.* **117,** 1–30.

Chiou, B. S., and R. R. Youngs (2008). An NGA model for the average horizontal component of peak ground motion and response spectra, *Earthq. Spectra* **24,** 173–215.

Chiou, B. S. J., and R. R. Youngs (2014). Update of the Chiou and Youngs NGA model for the average horizontal component of peak ground motion and response spectra, *Earthq. Spectra* **30,** 1117–1153.

Crempien, J. G. F., and R. J. Archuleta (2015). UCSB method for simulation of broadband ground motion from kinematic earthquake sources, *Seismol. Res. Lett.* **86,** 61–67.

Donahue, J. L., and N. Abrahamson (2014). Simulation-based hanging wall effects, *Earthq. Spectra* **30,** 1269–1284.

Flesch, L. M., W. E. Holt, A. J. Haines, and B. Shen-tult (2000). Dynamics of the Pacific–North American plate boundary in the western United States, *Science* **287,** 3–5.

Frankel, A. (2009). A constant stress-drop model for producing broadband synthetic seismograms: Comparison with the Next Generation Attenuation relations, *Bull. Seismol. Soc. Am.* **99,** 664–680.

Goulet, C. A., N. A. Abrahamson, P. G. Somerville, and K. E. Wooddell (2015). The SCEC broadband platform validation exercise: Methodology for code validation in the context of seismic-hazard analyses, *Seismol. Res. Lett.* **86**.

Graves, R., and A. Pitarka (2015). Refinements to the Graves and Pitarka (2010) broadband ground-motion simulation method, *Seismol. Res. Lett.* **86,** 75–80.

Graves, R., and A. Pitarka (2016). Kinematic ground motion simulations on rough faults including effects of 3D stochastic velocity perturbations, *Bull. Seismol. Soc. Am.* **106,** 2136–2153.

Harris, R. A., M. Barall, R. Archuleta, B. Aagaard, J. P. Ampuero, H. Bhat, L. Dalguer, P. Dawson, S. Day, G. Ely, *et al.* (2009). The SCEC/USGS dynamic earthquake rupture code verification exercise, *Seismol. Res. Lett.* **80,** 119–126.

Hartzell, S., M. Guatteri, P. M. Mai, P.-C. Liu, and M. Fisk (2005). Calculation of broadband time histories of ground motion, part II: Kinematic and dynamic modeling using theoretical Green's functions and comparison with the 1994 Northridge earthquake, *Bull. Seismol. Soc. Am.* **95,** 614–645.

Hartzell, S., S. Harmsen, and A. Frankel (2010). Effects of 3D random correlated velocity perturbations on predicted ground motions, *Bull. Seismol. Soc. Am.* **100,** 1415–1426.

Hoek, E., and E. Brown (1997). Practical estimates of rock mass strength, *Int. J. Rock Mech. Min. Sci.* **34,** 1165–1186.

Lee, E., and P. Chen (2014). Full-3-D tomography for crustal structure in Southern California based on the scattering-integral and the adjoint-wavefield methods, *J. Geophys. Res.* **119,** 6421–6451.

Mai, P. M., W. Imperatori, and K. B. Olsen (2010). Hybrid broadband ground-motion simulations: Combining long-period deterministic synthetics with high-frequency multiple *S*-to-*S* backscattering, *Bull. Seismol. Soc. Am.* **100,** 2124–2142.

Nakata, N., and G. C. Beroza (2015). Stochastic characterization of mesoscale seismic velocity heterogeneity in Long Beach, California, *Geophys. J. Int.* **203,** 2049–2054.

Olsen, K. B. (2000). Site amplification in the Los Angeles basin from three-dimensional modeling of ground motion, *Bull. Seismol. Soc. Am.* **90,** S77–S94.

Olsen, K. B., and R. Takedatsu (2015). The SDSU broadband ground-motion generation module BBtoolbox version 1. 5, *Seismol. Res. Lett.* **86,** 81–88.

Rodriguez-Marek, A., F. Cotton, N. A. Abrahamson, S. Akkar, L. A. Atik, B. Edwards, G. A. Montalva, and H. M. Dawood (2013). A model for single-station standard deviation using data from various tectonic regions, *Bull. Seismol. Soc. Am.* **103,** 3149–3163.

Roten, D., K. B. Olsen, and S. Day (2017). Off-fault deformations and shallow slip deficit from dynamic rupture simulations, *Geophys. Res. Lett.* **44,** 7733–7742.

Roten, D., K. B. Olsen, S. M. Day, Y. Cui, and D. Fäh (2014). Expected seismic shaking in Los Angeles reduced by San Andreas fault zone plasticity, *Geophys. Res. Lett.* **41,** 2769–2777.

Roten, D., K. B. Olsen, and J. C. Pechmann (2012). 3D simulations of M 7 earthquakes on the Wasatch fault, Utah, part II: Broadband (0–10 Hz) ground motions and nonlinear soil behavior, *Bull. Seismol. Soc. Am.* **102,** 2008–2030.

Roten, D., K. B. Olsen, J. C. Pechmann, and H. Magistrale (2011). 3D Simulations of M 7 earthquakes on the Wasatch fault, Utah, part I: Long-period (0–1 Hz) ground motion, *Bull. Seismol. Soc. Am.* **101,** 2045–2063.

Savran, W. H., and K. B. Olsen (2016). Model for small-scale crustal heterogeneity in Los Angeles basin based on inversion of sonic log data, *Geophys. J. Int.* **205,** 856–863.

Shahi, S. K., and J. W. Baker (2014). NGA-West2 models for ground motion directionality, *Earthq. Spectra* **30,** 1285–1300.

Shi, Z., and S. M. Day (2013). Rupture dynamics and ground motion from 3-D rough-fault simulations, *J. Geophys. Res.* **118,** 1122–1141.

Townend, J., and M. Zoback (2004). Regional tectonic stress near the San Andreas fault in central and southern California, *Geophys. Res. Lett.* **31,** 1–5.

Wald, D. J., T. H. Heaton, and K. W. Hudnut (1996). The slip history of the 1994 Northridge, California, earthquake determined from strong-motion, teleseismic, GPS, and leveling data, *Bull. Seismol. Soc. Am.* **86,** 49–70.

Withers, K. B., K. B. Olsen, and S. M. Day (2015). Memory-efficient simulation of frequency-dependent *Q*, *Bull. Seismol. Soc. Am.* **105,** 3129–3142.

Withers, K. B., K. B. Olsen, S. M. Day, and Z. Shi (2018). Ground motion and intraevent variability from 3D deterministic broadband (0–7.5 Hz) simulations along a nonplanar strike-slip fault, *Bull. Seismol. Soc. Am.* doi: 10.1785/0120180006.

Department of Geological Science
5500 Campanile Drive
San Diego State University
San Diego, California 92182
kwithers@usgs.gov
kbolsen@sdsu.edu
sday@sdsu.edu
(K.B.W., K.B.O., S.M.D.)

Tokio Marine Technologies LLC
2160 Satellite Boulevard 400
Duluth, Georgia 30097
samzqshi@gmail.com
(Z.S.)

Manuscript received 8 January 2018;
Published Online 13 November 2018